Energy & Environmental Science

COMMUNICATION

View Article Online
View Journal | View Issue

Cite this: *Energy Environ. Sci.*, 2016, 9, 2563

Received 4th May 2016,
Accepted 6th July 2016

DOI: 10.1039/c6ee01297c

www.rsc.org/ees

Nitrogen-doped cobalt phosphate@nanocarbon hybrids for efficient electrocatalytic oxygen reduction†

Tianhua Zhou,[a] Yonghua Du,[b] Shengming Yin,[a] Xuezeng Tian,[c] Hongbin Yang,[a] Xin Wang,[a] Bin Liu,[a] Haimei Zheng,[c] Shizhang Qiao*[de] and Rong Xu*[af]

The development of efficient non-noble metal electrocatalysts for the oxygen reduction reaction (ORR) is still highly desirable before non-noble metal catalysts can replace platinum catalysts. Herein, we have synthesized a new type of ORR catalyst, $Co_3(PO_4)_2$C-N/rGOA, containing N-coordinated cobalt phosphate, through the thermal treatment of a phosphonate-based metal–organic framework (MOF). $Co_3(PO_4)_2$C-N/rGOA exhibits not only a comparable onset potential and half-wave potential but also superior stability to the commercial Pt/C catalyst for the ORR in alkaline solutions (0.1 and 1.0 M KOH). A combination of structural characterization (*e.g.*, XPS, HRTEM, XANES, and EXAFS) and electrochemical analysis shows that the high ORR activity of the $Co_3(PO_4)_2$C-N/rGOA catalyst should be attributed to the co-existence of N-doped graphitic carbon and the cobalt phosphate with Co–N species that boost the activity of the cobalt phosphate. These findings open an avenue for exploring the use of phosphonate-based MOFs for energy conversion and storage applications.

Broader context

The development of non-noble metal catalysts with oxygen reduction reaction (ORR) activity has been a hot topic in the area of fuel cells and lithium-air batteries. Great effort has been devoted to the synthesis of heteroatom (*e.g.*, nitrogen and/or phosphorus, boron, sulfur) doped nanostructured carbon materials. Among these heteroatom-doped materials, N-doped carbon hybrid materials have been considered as promising candidates for the ORR due to their high electrocatalytic activity and excellent durability. However, the nature of the active sites still remains unclear. Herein, we report a phosphonate-based metal–organic framework (MOF) derived cobalt phosphate/graphene hybrid as a highly efficient electrocatalyst for the ORR under alkaline conditions. A combination of electrochemical, X-ray photoelectron spectroscopy (XPS) and X-ray absorption spectroscopy (XAS) techniques uncovers that the Co–N coordination of cobalt phosphate efficiently boosts the ORR activity and the resultant hybrid materials display comparable activity to Pt/C in terms of half-wave potential, but display superior stability to Pt/C in 0.1 and 1.0 M KOH solutions. This work not only provides a firm starting point for the further development of a new class of ORR catalysts derived from phosphonate-based MOFs but also new clues to explore their application in energy conversion systems.

Introduction

The development of efficient catalysts for the oxygen reduction reaction (ORR) is one of the keys to the realization of the renewable energy applications of proton exchange membrane fuel cells (PEMFCs).[1] Due to the sluggish kinetics of the ORR, the cathode side generally requires the utilization of noble metal catalysts, predominantly platinum (Pt) and its alloys.[2,3] Although they are the most efficient and commercially available electrocatalysts for the ORR, high cost and poor long-term stability may hamper their practical usage.[4,5] Alternatively, nitrogen-doped transition metals (Co, Mn, Fe, *etc.*), besides metal-free carbon materials, are extensively studied as effective candidates for the ORR,[6,7] most of which are synthesized by the pyrolysis of complexes containing $M–N_4$ moieties (M = Fe or Co).[4,8–10] The active sites are often attributed to be some form of $M–N_x$. Nonetheless, it remains elusive whether different types of nitrogen-doped transition metal/carbon catalysts should necessarily have the same structure of active sites.[9,10] Despite the uncertainty, the development of new non-noble metal electrocatalysts is still highly desirable before nonprecious metal catalysts can replace platinum catalysts.

Recently, transition metal phosphates have attracted extensive interest for energy conversion and storage applications due to their

[a] *School of Chemical & Biomedical Engineering, Nanyang Technological University, 62 Nanyang Drive, Singapore 637459. E-mail: rxu@ntu.edu.sg*
[b] *Institute of Chemical and Engineering Sciences, 1 Pesek Road, Jurong Island, 627833, Singapore*
[c] *Materials Sciences Division, Lawrence Berkeley National Laboratory, Berkeley, California, 94720, USA*
[d] *School of Chemical Engineering, The University of Adelaide, Adelaide, SA 5005, Australia. E-mail: s.qiao@adelaide.edu.au*
[e] *School of Materials Science and Engineering, Tianjin University, 300072, Tianjin, P. R. China*
[f] *SinBeRISE CREATE, National Research Foundation, CREATE Tower level 11, 1 Create Way, 138602, Singapore*

† Electronic supplementary information (ESI) available: Experimental method and supporting material. See DOI: 10.1039/c6ee01297c

high stability and catalytic efficiency.[11–15] They can not only drive water oxidation but also influence the electrocatalytic oxygen reduction activity of supported noble metals.[15,16] Catalysts composed of Pt on metal phosphates have been reported to exhibit improved ORR performance and durability compared to commercial Pt/C.[12,14,16–17] Although a large number of catalytic systems display improved performance, research is mainly focused on costly metals as the core elements, such as Au and Pt,[12,14,16–18] whereas it remains unclear whether transition metal phosphates alone would be efficient ORR catalysts. It is worth noting that phosphonate-based metal–organic frameworks (MOFs) have been developed as promising new candidates for proton conductors.[19–23] Moreover, theoretical studies also indicate that the phosphate group plays a crucial role in proton transport, which is of fundamental importance not only for the proton exchange membrane in PEMFCs but also in catalysing the ORR.[24,25] Thus, the rational design and fabrication of transition metal phosphates as ORR catalysts can provide a firm starting point for the development of a new class of ORR catalysts. However, only a few hybrids consisting of cobalt and phosphate have been applied to the ORR.[26]

To this end, it is imperative to synthesize highly efficient ORR catalysts based on nonprecious metal phosphates with catalytic performances close to or better than those of noble metals. As previously reported, cobalt-based materials have been extensively designed to catalyze the ORR.[27–30] Due to their high tendency for aggregation and low conductivity, cobalt or cobalt oxide nanoparticles are usually decorated with conducting carbon materials, such as carbon nanotubes and graphene, to improve their catalytic activity.[31,32] Especially, nitrogen-doped graphitic nanocarbon formed *in situ*, which is derived from a nitrogen-containing polymer (*e.g.*, polyaniline) or metal–organic frameworks (MOFs) by means of high-temperature thermal treatment, is found to be crucial for ORR activity and stability enhancement.[10,33–37] These highly ordered graphitic carbon materials serve as a robust support for hosting the active sites.[35] The coupling between carbon and the catalyst nanoparticles can modify the electronic structure and facilitate electron transfer at the interface.

Herein, we report a new hybrid ORR catalyst, composed of N-coordinated cobalt phosphate supported on a rGO sheet ($Co_3(PO_4)_2$C-N/rGOA), through pyrolysis of a mixture of graphene oxide and a cobalt phosphonate-based MOF. When used as an ORR catalyst, $Co_3(PO_4)_2$C-N/rGOA shows comparable half-wave and onset potentials to those of a Pt/C catalyst, as well as a small Tafel slope with long-term stability in alkaline media. Experimental observations indicate that the catalytic activity originates from N-coordinated cobalt phosphate and N-doped graphitic nanocarbon hybrids. To the best of our knowledge, this is the first report on the use of phosphonate-based MOF derived $Co_3(PO_4)_2$ as a highly active catalyst for the ORR.

Results and discussion

Our strategy for the synthesis of the $Co_3(PO_4)_2$C-N/rGOA catalyst is shown in Scheme S1 (ESI†). Firstly, a phosphonate-based MOF precursor, $Co_3(O_3PCH_2–NC_4H_7–CO_2)_2{\cdot}4H_2O$ (referred to as SH_3LCo), was prepared from a bio-inspired chiral organic phosphonic acid ligand, namely, *N*-(phosphonomethyl)proline (referred to as SH_3L), according to our previous report.[38] Then the phosphonate-based MOF was deposited on graphene oxide. The resulting mixture was annealed at 800 °C under a nitrogen atmosphere for 3 h followed by calcination at 250 °C for 1.5 h in air. Finally, the pyrolysis products were soaked in acid solution to remove unstable cobalt species. The as-obtained sample is denoted $Co_3(PO_4)_2$C-N/rGOA. For comparison, a metal-free carbon catalyst (referred to as PNrGO) with N and P co-doped carbon was also prepared using graphene oxide and the SH_3L ligand as the precursors through the same procedure as for $Co_3(PO_4)_2$C-N/rGOA.

Fig. 1a shows low-magnification transmission electron microscopy (TEM) and high angle annular dark field (HAADF) scanning transmission electron microscopy (STEM) images, indicating the MOF derived cobalt nanoparticles are uniformly embedded in the carbon sheet. The high-resolution (HR) TEM image in Fig. 1b reveals the high crystallinity of the cobalt phosphate nanocrystal. The corresponding fast Fourier transform (FFT) image (Fig. 1c) can be indexed to a monoclinic $Co_3(PO_4)_2$ structure (space group of $P2_1/c$, a = 7.56 Å, b = 8.37 Å, c = 5.06 Å, and β = 94.03°). STEM-energy dispersive X-ray spectroscopy (EDS) elemental mapping also suggests a uniform distribution of C, P, O, N and Co in the hybrid material (Fig. 1e). As shown in Fig. 1d, a hollow sphere-like carbon nanoshell is observed, indicating that some nanoparticles are removed during acid treatment. This observation provides evidence that the presence of a graphitic carbon shell formed *in situ* surrounds the cobalt nanoparticles and thus is favourable for the stability of the catalyst. More TEM images can be found in Fig. S1 (ESI†). Fig. S2 (ESI†) shows the nitrogen adsorption/desorption isotherm of $Co_3(PO_4)_2$C-N/rGOA, which displays a slightly higher BET surface area (30.1 $m^2\ g^{-1}$) than that of mildly oxidized graphene (19.6 $m^2\ g^{-1}$),[39] but one comparable to that of the precursor SH_3LCo. The structure and quality of the graphitic carbon materials were investigated using Raman spectroscopy (Fig. 2a). With the introduction of cobalt phosphate, the G band of $Co_3(PO_4)_2$C-N/rGOA shifts toward a lower wavenumber of 1564 cm^{-1} together with a decrease in the I_D/I_G ratio (0.44), in comparison to that of PNrGO without cobalt species (0.95); this indicates the formation of more ordered graphitic carbon due to the catalytic effect of cobalt species, which is helpful for stability and charge transfer.[29,35,40–42]

The structure of $Co_3(PO_4)_2$C-N/rGOA was further characterized using X-ray diffraction (XRD) techniques (Fig. 2b). The peaks are consistent with those of monoclinic phase $Co_3(PO_4)_2$, verifying the transformation of SH_3LCo to $Co_3(PO_4)_2$ in agreement with the TEM results. A strong diffraction peak observed at 25.9°, corresponding to a d-spacing of 0.34 nm, is attributed to the overlapping diffraction of the graphitic carbon shell formed *in situ*, rGO and cobalt phosphate. X-ray photoelectron spectroscopy (XPS) results indicate the presence of C, N, O, Co and P elements on the surface of the sample (Fig. S3, ESI†). To better determine the bonding states of nitrogen and cobalt, the metal-free PNrGO and the pristine SH_3LCo crystal were also studied as references. The N 1s spectrum of PNrGO presents three types of nitrogen

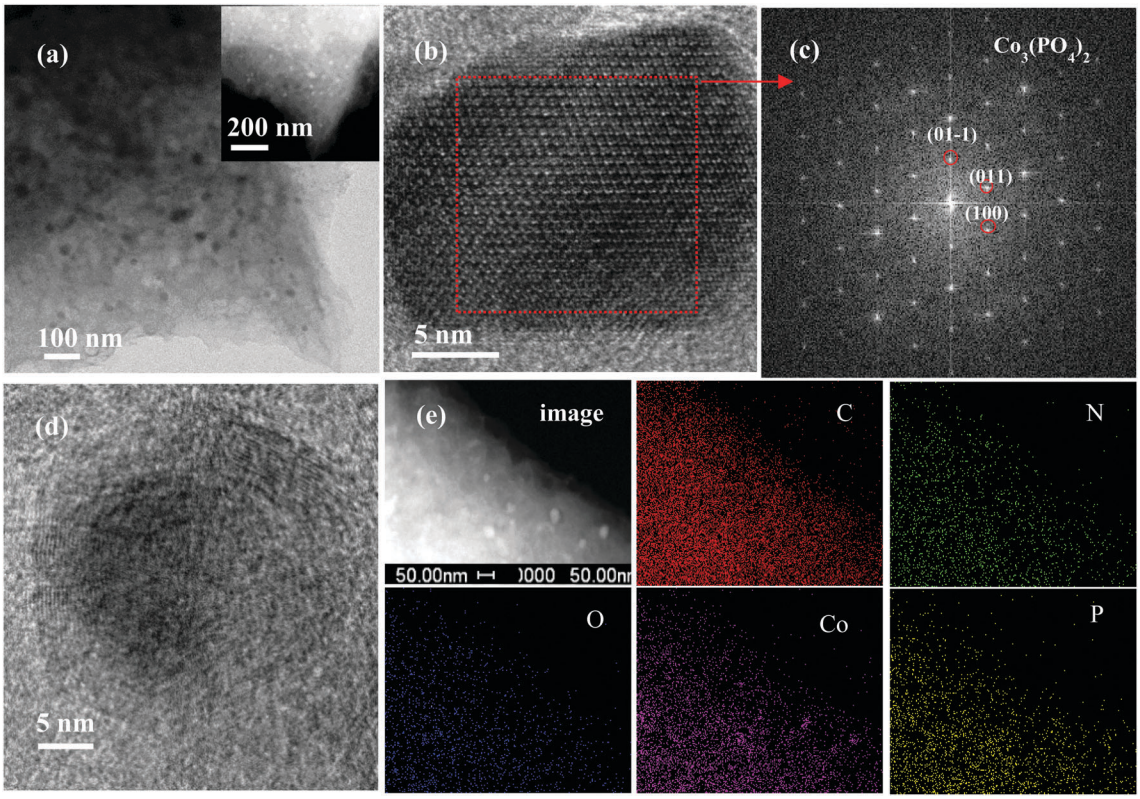

Fig. 1 (a) TEM and (b) HRTEM images of $Co_3(PO_4)_2$C-N/rGOA, (c) fast Fourier transform (FFT) of the nanocrystal structure in (b) and (d) HRTEM of hollow nanoshells, and (e) STEM and corresponding elemental mapping images of $Co_3(PO_4)_2$C-N/rGOA, indicating the distribution of C, P, O, N and Co. Inset of (a): HAADF-STEM image of $Co_3(PO_4)_2$C-N/rGOA.

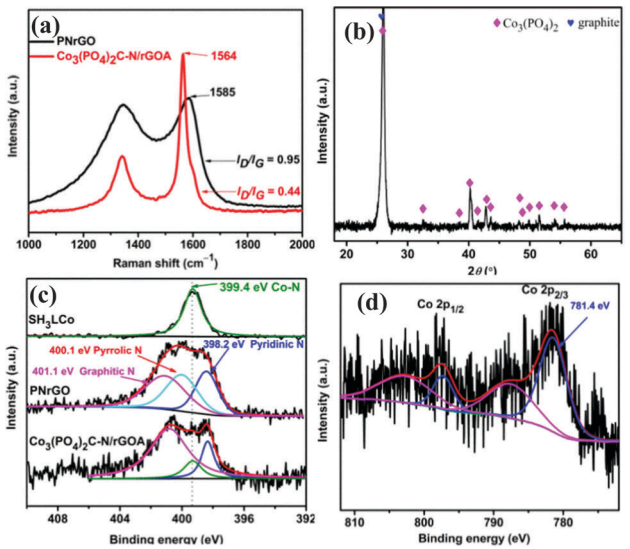

Fig. 2 (a) Raman (λ_{ex} = 514 nm) spectra of $Co_3(PO_4)_2$C-N/rGOA and PNrGO, (b) XRD pattern of $Co_3(PO_4)_2$C-N/rGOA, (c) N 1s XPS spectra of $Co_3(PO_4)_2$C-N/rGOA, PNrGO and SH_3LCO, and (d) Co 2p XPS spectrum of $Co_3(PO_4)_2$C-N/rGOA.

species, which are assigned to pyridinic (398.2 eV), pyrrolic (400.1 eV), and graphitic (401.1 eV) nitrogen atoms according to their binding energies (Fig. 2c).[43,44] On the other hand, the N 1s spectrum of $Co_3(PO_4)_2$C-N/rGOA can be deconvoluted to three peaks at 398.2, 399.4, and 401.0 eV (Fig. 2c). Similarly, the peaks at around 398.2 and 401.0 eV are attributed to the above-assigned pyridinic and graphitic nitrogen. After the introduction of cobalt, the peak at 400.1 eV associated with pyrrolic N disappears, while a new peak at 399.4 eV is observed for $Co_3(PO_4)_2$C-N/rGOA, implying the formation of nitrogen species similar to the Co–N coordination in the SH_3LCo crystal (Fig. 2c).[45] This observation demonstrates that the Co–N bond is retained after the high-temperature treatment of SH_3LCo. Furthermore, the Co 2p spectrum of $Co_3(PO_4)_2$C-N/rGOA displays the binding energies of the Co $2p_{3/2}$ and Co $2p_{1/2}$ peaks at 781.4 eV and 797.2 eV, with their corresponding satellite peaks at 787.6 eV and 802.7 eV, respectively (Fig. 2d). These binding energies are characteristic of Co(II) in the hybrid material. Compared with the peak at 780.2 eV corresponding to Co $2p_{3/2}$ in the SH_3LCo crystal, a slight shift to a higher binding energy (781.4 eV) in $Co_3(PO_4)_2$C-N/rGOA should be due to the interaction between cobalt and the carbon besides nitrogen, resulting in a weakening of the electron density in the cobalt atoms. The spectrum of P 2p at 133.2 eV is assigned to P–O species (Fig. S3, ESI†). The above observations collectively demonstrate that N-doped $Co_3(PO_4)_2$ carbon hybrid material has been successfully prepared by means of thermal treatment.

The electrocatalytic activity of $Co_3(PO_4)_2$C-N/rGOA was first evaluated using cyclic voltammetry (CV) in 0.1 M KOH solution.

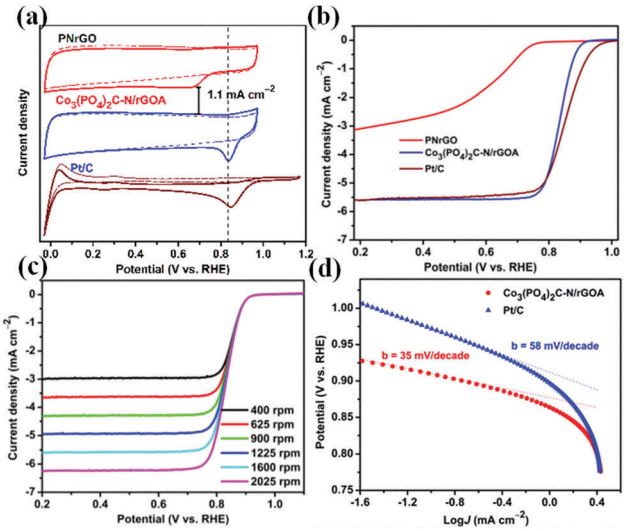

Fig. 3 (a) CV curves of $Co_3(PO_4)_2C$-N/rGOA, PNrGO and commercial Pt/C in Ar (dotted lines) and O_2-saturated (solid lines) 0.1 M KOH solution at a scan rate of 20 mV s^{-1}. (b) LSV curves of $Co_3(PO_4)_2C$-N/rGOA, PNrGO and Pt/C at a rotation rate of 1600 rpm and a scan rate of 5 mV s^{-1}. (c) RDE curves of $Co_3(PO_4)_2C$-N/rGOA at various rotation rates at a scan rate of 5 mV s^{-1}. (d) Tafel plots of $Co_3(PO_4)_2C$-N/rGOA and Pt/C. The loading of catalyst was 20 μg_{Pt} cm^{-2} for Pt/C and 0.25 mg cm^{-2} for cobalt-based catalysts.

Commercial Pt/C and PNrGO without Co were also examined for comparison. The CV curves in Fig. 3a show an obvious oxygen reduction peak for samples in the O_2-saturated solution, whereas no perceptible voltammetric current was observed in the presence of Ar. Interestingly, by comparing the CV curves of PNrGO and $Co_3(PO_4)_2C$-N/rGOA, it is found that a slightly active N and P-doped carbon catalyst becomes highly active with the incorporation of cobalt, demonstrating the crucial role of the Co species. As shown in Fig. 3a, the ORR cathodic peak of the $Co_3(PO_4)_2C$-N/rGOA electrode is at 0.837 V *vs.* RHE, only 9 mV more negative than that of commercial Pt/C (peak potential at 0.846 V). The electrocatalytic activity of $Co_3(PO_4)_2C$-N/rGOA was further evaluated using linear sweep voltammetry (LSV) curves obtained with a rotating disk electrode (RDE) in O_2-saturated 0.1 M KOH solution, at a scan rate of 5 mV s^{-1} and a rotating rate of 1600 rpm. As shown in Fig. 3b, the onset potential for $Co_3(PO_4)_2C$-N/rGOA (0.962 V) is about 46 mV more negative than that of Pt/C (1.008 V) while the half-wave potential (0.837 V) is slightly smaller than that of Pt/C (0.851 V). RDE measurements (Fig. 3c) reveal an electron transfer number of ~4.0 at 0.60–0.75 V on the basis of Koutecky–Levich (K–L) plots (Fig. S4, ESI†), suggesting that the $Co_3(PO_4)_2C$-N/rGOA catalyst favours a four-electron transfer process toward the ORR and O_2 is reduced to OH^-. Interestingly, the kinetic current density based on the intercept of the K–L plot at different potential values is comparable to that of commercial Pt/C (Fig. S4 and Table S1, ESI†). Furthermore, the Tafel slope (35 mV decade^{-1}) is also significantly smaller than that of Pt/C (58 mV decade^{-1}) in 0.1 M KOH solution (Fig. 3d). The value is close to 2.303 ($2RT/3F$) V decade^{-1} (where R is the universal gas constant and F is the Faraday constant), indicating that the rate-limiting step could be the protonation of O_2^- at the active centers.[27,46,47] These results suggest the high intrinsic activity and favourable kinetics of $Co_3(PO_4)_2C$-N/rGOA (Table S2, ESI†).

The ORR activity of $Co_3(PO_4)_2C$-N/rGOA was further observed in 1.0 M KOH electrolyte. Both CV and RDE measurements reveal that the $Co_3(PO_4)_2C$-N/rGOA catalyst shows high electrocatalytic activity with a greater positive onset potential (~0.968 V) and half-wave potential (0.872 V) than those of $Co_3(PO_4)_2C$-N/rGOA in 0.1 M KOH, which matches the performance of freshly prepared Pt/C with a loading of 0.1 mg cm^{-2} or a loading of 0.25 mg cm^{-2} (0.872 V) (Fig. 4a–c4, and Fig. S5, ESI†). Rotating ring-disk electrode (RRDE) measurements on a $Co_3(PO_4)_2C$-N/rGOA electrode were carried out to determine the ORR pathway. Fig. 4 shows the disk and ring currents collected at 1600 rpm in 1.0 M KOH. The H_2O_2 yield obtained using RRDE measurements is below 6% over the potential range of 0.6 to 0.8 V, affording an electron number of ~4.0 (Fig. 4d and Fig. S6, ESI†), in line with the result obtained from the K–L plot on the basis of the RDE experiments (Fig. 4c). Hence, the results from RRDE and

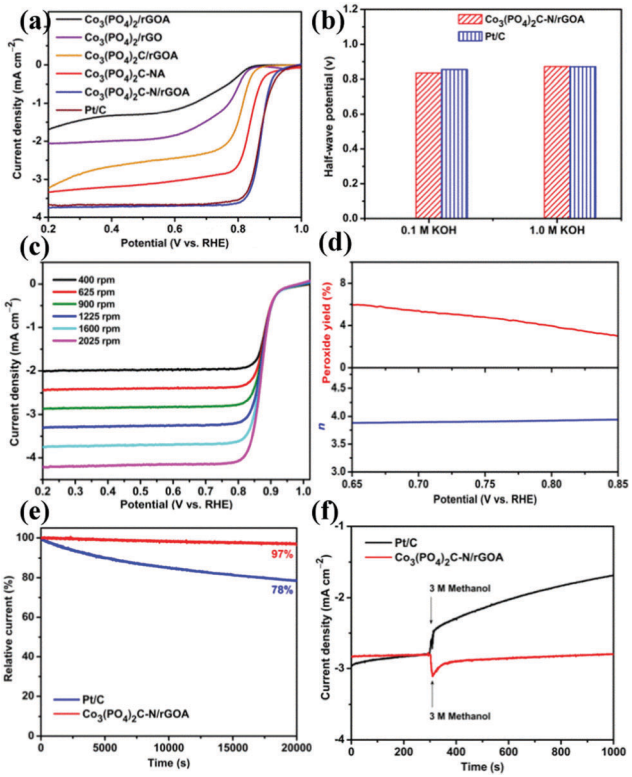

Fig. 4 (a) LSV curves of cobalt phosphate hybrid materials and Pt/C in 1.0 M KOH solution. (b) Half-wave potentials from the LSV curves for $Co_3(PO_4)_2C$-N/rGOA and Pt/C. (c) RDE curves of $Co_3(PO_4)_2C$-N/rGOA at various rotation rates with a scan rate of 5 mV s^{-1}. (d) Peroxide yield (%) and electron transfer number (n) for $Co_3(PO_4)_2C$-N/rGOA at various potentials, based on the corresponding RRDE data. (e) Chronoamperometric curves of $Co_3(PO_4)_2C$-N/rGOA and Pt/C kept at 0.8 V *vs.* RHE. (f) Chronoamperometric responses of Pt/C and $Co_3(PO_4)_2C$-N/rGOA at 0.8 V to the addition of 3.0 M methanol into an O_2-saturated 1.0 M KOH solution. For all RDEs, the loading of catalyst was 20 μg_{pt} cm^{-2} for Pt/C and 0.25 mg cm^{-2} for cobalt-based catalysts. All tests were performed in O_2-saturated 1.0 M KOH with a scan rate of 5 mV s^{-1} unless otherwise stated.

RDE measurements also convince that there is a mainly four-electron reaction pathway in 1.0 M KOH electrolyte. In addition, $Co_3(PO_4)_2$C-N/rGOA displays superior durability. The chronoamperometric measurements exhibit only a slight current loss with a high retention of more than 97% of the initial current even after 25 000 s of testing, whereas the commercial Pt/C catalyst suffers nearly 22% activity loss (Fig. 4e). Moreover, the ORR current density of $Co_3(PO_4)_2$C-N/rGOA remains almost the same with negligible change except for a slight oscillation after the addition of 3.0 M methanol (Fig. 4f). In contrast, the Pt/C catalyst shows a sharp current jump due to the methanol oxidation reaction. These results demonstrate the comparable activity, higher stability and better selectivity of $Co_3(PO_4)_2$C-N/rGOA compared to the commercial Pt/C catalyst and other cobalt-based catalysts reported (Tables S3 and S4, ESI†).

Considering that the $Co_3(PO_4)_2$C-N/rGOA catalyst contains N-doped graphitic carbon, cobalt phosphate and graphene, to better understand the effect of these components on the catalytic performance, four control samples were prepared according to the same procedure as for $Co_3(PO_4)_2$C-N/rGOA but using different, precursors. Firstly, $Co_3(PO_4)_2$/rGO without a carbon shell was prepared using commercial $Co_3(PO_4)_2$ as the precursor. XRD confirms that before acid treatment the crystal phase belongs to monoclinic $Co_3(PO_4)_2$ (Fig. S7a, ESI†). However, after acid treatment, ICP analysis results indicate that the $Co_3(PO_4)_2$ phase is almost removed with less than 0.1 wt% cobalt remaining in $Co_3(PO_4)_2$/rGOA (the second control sample), presumably due to a lack of protection from the carbon shell. On the contrary, for the third control sample, 1.92 wt% cobalt remains in $Co_3(PO_4)_2$C/rGOA which was prepared using a nitrogen-free phosphonate-based MOF (PPACo). Furthermore, HRTEM reveals the presence of flake-like graphitic carbon layers in $Co_3(PO_4)_2$C/rGOA, which is further confirmed through Raman spectrum with an I_D/I_G ratio of 0.62, which is smaller than that in $Co_3(PO_4)_2$/rGOA (0.91) (Fig. S8, ESI†). HAADF images also indicate that some nanoparticles remain in the hybrid material, which are confirmed to be $Co_3(PO_4)_2$ using HRTEM and elemental mapping results (Fig. S8, ESI†). These observations suggest that the graphitic carbon shell formed *in situ* from the decomposition of the organic ligand stabilizes the cobalt centres and plays an important role in protecting the active sites from leaching. For the last control sample, a N-doped cobalt phosphate graphitic carbon hybrid, $Co_3(PO_4)_2$C-NA, was obtained through the direct pyrolysis of SH_3LCo without graphene oxide. The XPS results for $Co_3(PO_4)_2$C-NA reveal that it has similar surface components to $Co_3(PO_4)_2$C-N/rGOA and shows the presence of four types of nitrogen species including pyridinic nitrogen (398.2 eV), Co–N_x (399.4 eV), graphitic nitrogen (400.9 eV) and oxidized N (405.3 eV) (Fig. S9, ESI†). However, TEM images indicate that the morphology of $Co_3(PO_4)_2$C-NA remains almost the same as that of the precursor with large sized rod-like nanoparticles due to lack of graphene as a support (Fig. S9, ESI†).

The RDE measurements indicate that $Co_3(PO_4)_2$/rGO without a carbon shell displays some ORR activity (Fig. 4a). After acid treatment, $Co_3(PO_4)_2$/rGOA shows much poorer activity. On the contrary, $Co_3(PO_4)_2$C/rGOA shows significantly improved ORR activity compared with $Co_3(PO_4)_2$/rGO without a carbon shell, with an onset potential of 0.89 V and a half-wave potential of 0.81 V. This improvement can be attributed to the effect of the highly conductive graphitic carbon shell formed *in situ*, which is helpful for facilitating fast electron transfer.[35–37,48] Furthermore, after the graphitic carbon shell is doped with nitrogen, $Co_3(PO_4)_2$C-NA, even without rGO, displays significant improvement, with an onset potential of 0.941 V and a half-wave potential of 0.834 V, compared with $Co_3(PO_4)_2$C/rGOA. This improvement is attributed to the effect of the nitrogen introduced into the catalyst.[37] However, the performance is still inferior to that of $Co_3(PO_4)_2$C-N/rGOA. The latter exhibits an onset potential (0.968 V) and half-wave potential (0.872 V) that are 27 and 38 mV more positive than the former, respectively. In addition, its limiting current density is also significantly higher than that of $Co_3(PO_4)_2$C-NA. These results show that the introduction of graphene significantly improves the activity by inducing the formation of small and well-dispersed nanoparticles and also causing higher electronic conductivity (Fig. S10, ESI†). Therefore, all of these observations collectively demonstrate that it is essential to simultaneously incorporate cobalt species, a graphitic carbon shell, nitrogen doping and rGO for realizing the efficient ORR activity in $Co_3(PO_4)_2$C-N/rGOA.

So far, various work has been reported on co-doping transition metal and nitrogen atoms to form metal–N–C catalysts with excellent ORR activities. For instance, a minute amount of Co–N–C can significantly boost the ORR activity. The active site was ascribed to be Co–N_x–C or CoN_x/C species.[5] However, it still remains unclear which component serves as the main contributor to the ORR activity in this work. To further explore the structure of the active sites, the $Co_3(PO_4)_2$C-N/rGOA catalyst was investigated using X-ray absorption near-edge structure (XANES) and extended X-ray absorption fine structure (EXAFS) spectroscopies. From the Co K-edge XANES spectra of samples and references (Fig. 5a), it can be observed that the overall spectrum of $Co_3(PO_4)_2$C-N/rGOA is obviously different from that of metallic cobalt and CoN_4C, which was obtained through the pyrolysis of cobalt phthalocyanine using the same procedure as for $Co_3(PO_4)_2$C-N/rGOA, indicating that no apparent metallic cobalt exists in $Co_3(PO_4)_2$C-N/rGOA. On the contrary, the Co K-edge XANES spectrum of $Co_3(PO_4)_2$C-N/rGOA is similar to that of the reference $Co_3(PO_4)_2$, and in particular, nearly identical to that of the phosphonate-based MOF precursor (SH_3LCo), demonstrating that these cobalt species have the same oxidation state and similar coordination environments. Furthermore, compared with the reference $Co_3(PO_4)_2$, both $Co_3(PO_4)_2$C-N/rGOA and SH_3LCo present significantly higher pre-edge absorption, at about 7709 eV, which could be attributed to low molecular symmetry.[49] Accordingly, both $Co_3(PO_4)_2$C-N/rGOA and SH_3LCo display a weaker and broader main edge peak, which could derive from a distorted structure due to low symmetry. This is probably caused by cobalt species embedded in the carbon framework,[50–52] where the metal centers remain coordinated to nitrogen and oxygen atoms, in agreement with the XPS results. The coordination environment of the Co atoms is further confirmed using Fourier transform (FT) k^3-weighted EXAFS spectra. As shown in Fig. 5b,

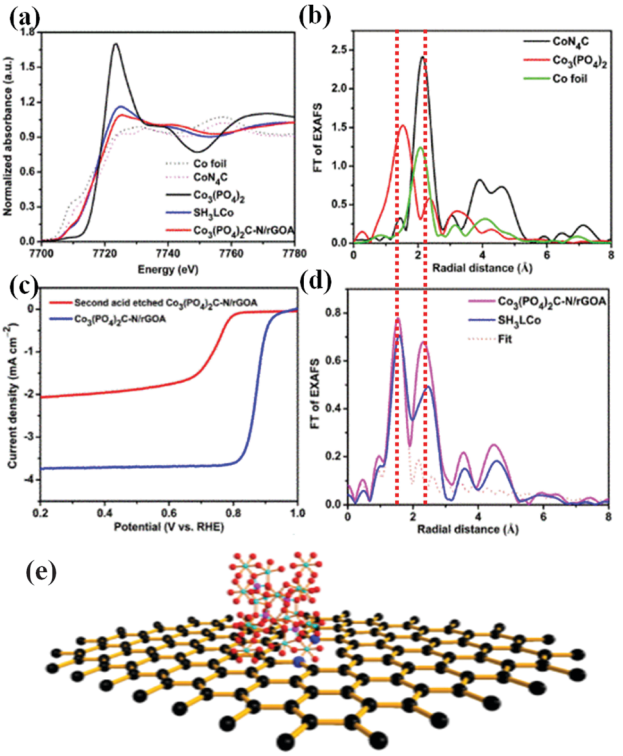

Fig. 5 (a) Normalized Co K-edge XANES spectra of $Co_3(PO_4)_2$C-N/rGOA and reference samples. (b) Co K-edge EXAFS spectra of $Co_3(PO_4)_2$C-N/rGOA and (d) its first-shell fitting curve. (c) LSV curves of $Co_3(PO_4)_2$C-N/rGOA and a second acid-etched sample at a rotation rate of 1600 rpm and a scan rate of 5 mV s^{-1} in 1.0 M KOH. (e) Structural model of $Co_3(PO_4)_2$C-N/rGOA.

there is significant difference among the spectra of metallic cobalt, CoN_4C and $Co_3(PO_4)_2$C-N/rGOA. On the contrary, the FT of the EXAFS spectrum of $Co_3(PO_4)_2$C-N/rGOA presents four distinguishable strong peaks, similar to that of SH_3LCo (Fig. 5d). The peak at 1.55 Å can be assigned to Co–N and Co–O first shell coordination, due to coordination of both nitrogen and oxygen to cobalt as observed in SH_3LCo, though the presence of nitrogen in the first shell coordination is not clearly distinguishable, probably due to the interference of two almost equal bond distances.[5] Their coordination numbers were estimated to be ~1 and ~5, respectively, based on the crystal structure of SH_3LCo (Table S5, ESI†). The second shell at 2.32 Å in the spectrum of $Co_3(PO_4)_2$C-N/rGOA is associated with a Co–Co contribution, which is slightly shorter than the Co–Co distance (2.47 Å) in SH_3LCo but is in good agreement with that of the reference $Co_3(PO_4)_2$. The second shell average distance R(Co–Co) shrinks in $Co_3(PO_4)_2$C-N/rGOA compared to in SH_3LCo, consistent with the unit cell volume shrinkage observed based on the crystal structure data ($Co_3(PO_4)_2$: V = 318.9 Å^3; SH_3LCo: V = 4385.0 Å^3). The next two peaks at 3.54 Å and 4.47 Å are likely derived from Co–Co–Co multiple scattering. The intense peaks suggest that the hybrid material has an extended structure, similar to SH_3LCo. Furthermore, the EXAFS spectrum of $Co_3(PO_4)_2$C-N/rGOA is also drastically different from that of Co–P/NC consisting of N-doped cobalt phosphide carbon material, which shows only a strong and broad peak located at about 1.81 Å.[53] It is worth noting that the metallic CoN_x could exist in minute amounts in the hybrid material, and its signals in XPS, XANES and EXAFS could be overwhelmed by those of cobalt phosphates. Thus it is difficult to verify the effect of metallic CoN_x using conventional measurements. To further clarify the issue, one more control experiment was performed. $Co_3(PO_4)_2$C-N/rGOA was further etched with an aqueous solution of 6 M HCl at room temperature for 48 h to remove the cobalt phosphate nanoparticles as much as possible. A combination of TEM, XPS and ICP (0.3 wt% Co remaining after etching) confirms that most of the cobalt phosphate was removed (Fig. S11, ESI†). As a result, the second acid-etched sample presents much inferior activity compared to the original $Co_3(PO_4)_2$C-N/rGOA (Fig. 5c), though XPS confirmed the presence of nitrogen and a small percentage of cobalt species after further etching (Fig. S11, ESI†). This result suggests that cobalt phosphate is necessary for $Co_3(PO_4)_2$C-N/rGOA to achieve efficient catalytic activity.

Based on the above observations, it is postulated that the presence of nitrogen-coordinated cobalt phosphate could be the main contributor to the remarkable capability of $Co_3(PO_4)_2$C-N/rGOA to catalyze the ORR with exceptional activity. In our study, the nitrogen-coordinated cobalt phosphate hybrid material is analogous to phosphate-stabilized Co–N clusters embedded in N-doped graphitic carbon materials (Fig. 5e). Phosphate groups not only stabilize the Co–N centers but also can deliver protons to enable proton-coupled electron transfer, facilitating the ORR process. The N-doped graphitic carbon formed *in situ* can not only directly serve as the active site for improved intrinsic activity, but also provide robust support to anchor the metal active sites for enhanced corrosion resistance to oxidative attack during the ORR.

Conclusions

In summary, we have synthesized a new type of phosphonate-based metal–organic framework derived cobalt phosphate hybrid carbon material with high activity toward the ORR in alkaline media. It is found that by using a nitrogen-containing metal–organic phosphonate as the precursor, an N-coordinated cobalt phosphate carbon hybrid material can be obtained. With the introduction of N-coordinated cobalt phosphate, the ORR catalytic activity can be improved significantly compared to cobalt phosphate without N-coordination. Our catalyst exhibits a high onset potential of 0.968 V and a half-wave potential of 0.872 V in 1.0 M KOH. It also shows superior stability compared to commercial Pt/C catalyst, and good tolerance to the methanol cross-over effect. The presence of N-doped graphitic carbon, cobalt phosphate with Co–N moieties and graphene having a suitable surface area in the hybrid material synergistically promotes the activity of the ORR. This work offers a new opportunity by using metal–organic phosphonate/metal phosphates as advanced catalysts for application in fuel cells and other electrochemical devices.

Acknowledgements

This research project is funded by the National Research Foundation (NRF), Prime Minister's Office, Singapore under its Campus

for Research Excellence and Technological Enterprise (CREATE) programme: The Singapore-Berkeley Research Initiative for Sustainable Energy (SinBeRISE). The authors greatly thank Prof. Z. Chen and Dr D. P. Wang for TEM measurements, Dr L. Zheng for the XANES and EXAFS experiments, Dr W. Yan for the BET experiments, and Dr B. Xia for discussion.

Notes and references

1 I. Moussallem, J. Jörissen, U. Kunz, S. Pinnow and T. Turek, *J. Appl. Electrochem.*, 2008, **38**, 1177–1194.
2 X. Huang, Z. Zhao, L. Cao, Y. Chen, E. Zhu, Z. Lin, M. Li, A. Yan, A. Zettl, Y. M. Wang, X. Duan, T. Mueller and Y. Huang, *Science*, 2015, **348**, 1230–1234.
3 D. Wang, H. L. Xin, R. Hovden, H. Wang, Y. Yu, D. A. Muller, F. J. DiSalvo and H. D. Abruña, *Nat. Mater.*, 2013, **12**, 81–87.
4 F. Jaouen, E. Proietti, M. Lefevre, R. Chenitz, J.-P. Dodelet, G. Wu, H. T. Chung, C. M. Johnston and P. Zelenay, *Energy Environ. Sci.*, 2011, **4**, 114–130.
5 R. Bashyam and P. Zelenay, *Nature*, 2006, **443**, 63–66.
6 K. Gong, F. Du, Z. Xia, M. Durstock and L. Dai, *Science*, 2009, **323**, 760–764.
7 L. Dai, Y. Xue, L. Qu, H.-J. Choi and J.-B. Baek, *Chem. Rev.*, 2015, **115**, 4823–4892.
8 J. Han, Y. J. Sa, Y. Shim, M. Choi, N. Park, S. H. Joo and S. Park, *Angew. Chem., Int. Ed.*, 2015, **54**, 12622–12626.
9 K. Strickland, E. Miner, Q. Jia, U. Tylus, N. Ramaswamy, W. Liang, M.-T. Sougrati, F. Jaouen and S. Mukerjee, *Nat. Commun.*, 2015, **6**, 7343–7350.
10 A. Zitolo, V. Goellner, V. Armel, M.-T. Sougrati, T. Mineva, L. Stievano, E. Fonda and F. Jaouen, *Nat. Mater.*, 2015, **14**, 937–942.
11 D. González-Flores, I. Sánchez, I. Zaharieva, K. Klingan, J. Heidkamp, P. Chernev, P. W. Menezes, M. Driess, H. Dau and M. L. Montero, *Angew. Chem., Int. Ed.*, 2015, **54**, 2472–2476.
12 Y. Park, B. Lee, C. Kim, J. Kim, S. Nam, Y. Oh and B. Park, *J. Phys. Chem. C*, 2010, **114**, 3688–3692.
13 H. Wang, Y. Yang, Y. Liang, L.-F. Cui, H. Sanchez Casalongue, Y. Li, G. Hong, Y. Cui and H. Dai, *Angew. Chem., Int. Ed.*, 2011, **50**, 7364–7368.
14 C. Kim, B. Lee, Y. Park, B. Park, J. Lee and H. Kim, *Appl. Phys. Lett.*, 2007, **91**, 113101.
15 M. W. Kanan and D. G. Nocera, *Science*, 2008, **321**, 1072–1075.
16 P. J. Bouwman, W. Dmowski, J. Stanley, G. B. Cotten and K. E. Swider-Lyons, *J. Electrochem. Soc.*, 2004, **151**, A1989–A1998.
17 Y. Park, S. Nam, Y. Oh, H. Choi, J. Park and B. Park, *J. Phys. Chem. C*, 2011, **115**, 7092–7096.
18 J. Védrine, *Top. Catal.*, 2000, **11–12**, 147–152.
19 K. J. Gagnon, H. P. Perry and A. Clearfield, *Chem. Rev.*, 2012, **112**, 1034–1054.
20 J. M. Taylor, R. K. Mah, I. L. Moudrakovski, C. I. Ratcliffe, R. Vaidhyanathan and G. K. H. Shimizu, *J. Am. Chem. Soc.*, 2010, **132**, 14055–14057.
21 S. Pili, S. P. Argent, C. G. Morris, P. Rought, V. García-Sakai, I. P. Silverwood, T. L. Easun, M. Li, M. R. Warren, C. A. Murray, C. C. Tang, S. Yang and M. Schröder, *J. Am. Chem. Soc.*, 2016, **138**, 6352–6355.
22 J. M. Taylor, K. W. Dawson and G. K. H. Shimizu, *J. Am. Chem. Soc.*, 2013, **135**, 1193–1196.
23 M. Bazaga-García, R. M. P. Colodrero, M. Papadaki, P. Garczarek, J. Zoń, P. Olivera-Pastor, E. R. Losilla, L. León-Reina, M. A. G. Aranda, D. Choquesillo-Lazarte, K. D. Demadis and A. Cabeza, *J. Am. Chem. Soc.*, 2014, **136**, 5731–5739.
24 R. Vuilleumier and D. Borgis, *Nat. Chem.*, 2012, **4**, 432–433.
25 L. Vilčiauskas, M. E. Tuckerman, G. Bester, S. J. Paddison and K.-D. Kreuer, *Nat. Chem.*, 2012, **4**, 461–466.
26 Z.-G. Zhao, J. Zhang, Y. Yuan, H. Lv, Y. Tian, D. Wu and Q.-W. Li, *Sci. Rep.*, 2013, **3**, 2263–2268.
27 Y. Liang, Y. Li, H. Wang, J. Zhou, J. Wang, T. Regier and H. Dai, *Nat. Mater.*, 2011, **10**, 780–786.
28 M. Yuasa, A. Yamaguchi, H. Itsuki, K. Tanaka, M. Yamamoto and K. Oyaizu, *Chem. Mater.*, 2005, **17**, 4278–4281.
29 Y.-Z. Chen, C. Wang, Z.-Y. Wu, Y. Xiong, Q. Xu, S.-H. Yu and H.-L. Jiang, *Adv. Mater.*, 2015, **27**, 5010–5016.
30 H.-W. Liang, W. Wei, Z.-S. Wu, X. Feng and K. Müllen, *J. Am. Chem. Soc.*, 2013, **135**, 16002–16005.
31 Y. Liang, Y. Li, H. Wang and H. Dai, *J. Am. Chem. Soc.*, 2013, **135**, 2013–2036.
32 S. Mao, Z. Wen, T. Huang, Y. Hou and J. Chen, *Energy Environ. Sci.*, 2014, **7**, 609–616.
33 H. Hu, L. Han, M. Yu, Z. Wang and X. W. Lou, *Energy Environ. Sci.*, 2016, **9**, 107–111.
34 W. Xia, R. Zou, L. An, D. Xia and S. Guo, *Energy Environ. Sci.*, 2015, **8**, 568–576.
35 G. Wu, K. L. More, C. M. Johnston and P. Zelenay, *Science*, 2011, **332**, 443–447.
36 J. Y. Cheon, J. H. Kim, J. H. Kim, K. C. Goddeti, J. Y. Park and S. H. Joo, *J. Am. Chem. Soc.*, 2014, **136**, 8875–8878.
37 D. Guo, R. Shibuya, C. Akiba, S. Saji, T. Kondo and J. Nakamura, *Science*, 2016, **351**, 361–365.
38 T. Zhou, D. Wang, S. Chun-Kiat Goh, J. Hong, J. Han, J. Mao and R. Xu, *Energy Environ. Sci.*, 2015, **8**, 526–534.
39 H.-X. Zhong, J. Wang, Y.-W. Zhang, W.-L. Xu, W. Xing, D. Xu, Y.-F. Zhang and X.-B. Zhang, *Angew. Chem., Int. Ed.*, 2014, **53**, 14235–14239.
40 Y. Meng, D. Voiry, A. Goswami, X. Zou, X. Huang, M. Chhowalla, Z. Liu and T. Asefa, *J. Am. Chem. Soc.*, 2014, **136**, 13554–13557.
41 L. Qu, Y. Liu, J.-B. Baek and L. Dai, *ACS Nano*, 2010, **4**, 1321–1326.
42 J. Tang, R. R. Salunkhe, J. Liu, N. L. Torad, M. Imura, S. Furukawa and Y. Yamauchi, *J. Am. Chem. Soc.*, 2015, **137**, 1572–1580.
43 Q. Li, P. Xu, W. Gao, S. Ma, G. Zhang, R. Cao, J. Cho, H.-L. Wang and G. Wu, *Adv. Mater.*, 2014, **26**, 1378–1386.
44 H. Wang, T. Maiyalagan and X. Wang, *ACS Catal.*, 2012, **2**, 781–794.

45 J. M. Ziegelbauer, T. S. Olson, S. Pylypenko, F. Alamgir, C. Jaye, P. Atanassov and S. Mukerjee, *J. Phys. Chem. C*, 2008, **112**, 8839–8849.
46 M. De Koninck and B. Marsan, *Electrochim. Acta*, 2008, **53**, 7012–7021.
47 R. Cao, R. Thapa, H. Kim, X. Xu, M. Gyu Kim, Q. Li, N. Park, M. Liu and J. Cho, *Nat. Commun.*, 2013, **4**, 2076–2082.
48 T. Y. Ma, S. Dai, M. Jaroniec and S. Z. Qiao, *J. Am. Chem. Soc.*, 2014, **136**, 13925–13931.
49 J. C. Swarbrick, T.-C. Weng, K. Schulte, A. N. Khlobystov and P. Glatzel, *Phys. Chem. Chem. Phys.*, 2010, **12**, 9693–9699.
50 Y. Gorlin, B. Lassalle-Kaiser, J. D. Benck, S. Gul, S. M. Webb, V. K. Yachandra, J. Yano and T. F. Jaramillo, *J. Am. Chem. Soc.*, 2013, **135**, 8525–8534.
51 D. J. Sprouster, R. Giulian, L. L. Araujo, P. Kluth, B. Johannessen, D. J. Cookson, G. J. Foran and M. C. Ridgway, *J. Appl. Phys.*, 2010, **107**, 014313.
52 D.-H. Ha, L. M. Moreau, C. R. Bealing, H. Zhang, R. G. Hennig and R. D. Robinson, *J. Mater. Chem.*, 2011, **21**, 11498–11510.
53 B. You, N. Jiang, M. Sheng, S. Gul, J. Yano and Y. Sun, *Chem. Mater.*, 2015, **27**, 7636–7642.

